Physics Letters B 792 (2019) 454–460

Contents lists available at ScienceDirect

Physics Letters B

www.elsevier.com/locate/physletb

Multiple chiral doublet bands with octupole correlations in reflection-asymmetric triaxial particle rotor model

Y.Y. Wang (王媛媛)[a], S.Q. Zhang (张双全)[b], P.W. Zhao (赵鹏巍)[b], J. Meng (孟杰)[b,a,c,*]

[a] School of Physics and Nuclear Energy Engineering, Beihang University, Beijing 100191, China
[b] State Key Laboratory of Nuclear Physics and Technology, School of Physics, Peking University, Beijing 100871, China
[c] Yukawa Institute for Theoretical Physics, Kyoto University, Kyoto 606-8502, Japan

ARTICLE INFO

Article history:
Received 1 February 2019
Received in revised form 21 February 2019
Accepted 8 April 2019
Available online 10 April 2019
Editor: J.-P. Blaizot

ABSTRACT

A reflection-asymmetric triaxial particle rotor model (RAT-PRM) with a quasi-proton and a quasi-neutron coupled with a reflection-asymmetric triaxial rotor is developed and applied to investigate the multiple chiral doublet (MχD) bands candidates with octupole correlations in ^{78}Br. The calculated excited energies, energy staggering parameters, and $B(M1)/B(E2)$ ratios are in a reasonable agreement with the data of the chiral doublet bands with positive- and negative-parity. It is found that both the triaxial deformation γ and octupole deformation β_3 influence the calculated $B(E1)$ values. The chiral geometry based on the angular momenta for the rotor, the valence proton and valence neutron is discussed in details.

1. Introduction

Chirality is a subject of general interests in natural science. Since the pioneering work of nuclear chirality by Frauendorf and Meng in 1997 [1], many efforts have been devoted to explore the chirality in atomic nuclei, see e.g., reviews [2–7].

The experimental signature of nuclear chirality is a pair of nearly degenerate $\Delta I = 1$ bands with the same parity, i.e., chiral doublet bands. In 2006, the multiple chiral doublets (MχD), i.e., more than one pair of chiral doublet bands in a single nucleus, is suggested based on the self-consistent covariant density functional theory (CDFT) [8]. The first experimental evidence for MχD is reported in ^{133}Ce [9], followed by ^{103}Rh [10], ^{78}Br [11], ^{136}Nd [12], and ^{195}Tl [13], etc. Up to now, 62 candidate chiral bands in 49 nuclei (including 9 nuclei with MχD) have been reported in the $A \sim 80$, 100, 130 and 190 mass regions [13–15].

Because of the observation of eight strong electric dipole ($E1$) transitions linking the positive- and negative-parity chiral bands [11], the MχD candidates observed in ^{78}Br provide the first example of chiral geometry in octupole soft nuclei and indicate that nuclear chirality can be robust against the octupole correlations. It also indicates that the chirality-parity quartet bands [2], which are a consequence of the simultaneous breaking of chiral and space-reflection symmetries, may exist in nuclei. The observations of MχD with octupole correlations and/or the possible chirality-parity quartet bands have brought severe challenges to current nuclear models and, thus, require the development of new approaches.

Theoretically, nuclear chirality has been investigated extensively with the triaxial particle rotor model (PRM) [1,16–20], the tilted axis cranking model (TAC) [1,21–24], the TAC approach with the random phase approximation [25,26] and the collective Hamiltonian [27–29], the interacting boson-fermion-fermion model [30], the generalized coherent state model [31] and the projected shell model [32–35], etc. The triaxial PRM is one of the most popular models for describing nuclear chirality as it is a quantal model coupling the collective rotation and the single-particle motions in the laboratory reference frame, and describes directly the quantum tunneling and energy splitting between the doublet bands.

In Ref. [11], the triaxial PRM calculation has been performed to describe the positive- and negative-parity chiral doublet bands observed in ^{78}Br with two individual configurations $\pi g_{9/2} \otimes \nu g_{9/2}$ and $\pi f_{5/2} \otimes \nu g_{9/2}$, respectively. The calculation supports the interpretation of the MχD with different parities [11]. However, the $E1$ linking transitions between the positive-parity band 1 and the negative-parity band 3 are not accessible in the triaxial PRM due to the omission of the octupole degree of freedom.

In this work, a reflection-asymmetric triaxial PRM (RAT-PRM) with both triaxial and octupole degrees of freedom is developed

* Corresponding author.
E-mail addresses: sqzhang@pku.edu.cn (S.Q. Zhang), mengj@pku.edu.cn (J. Meng).

https://doi.org/10.1016/j.physletb.2019.04.014

and applied to the MχD candidates with octupole correlations in ^{78}Br. The model is introduced in Sec. 2, and the numerical details are presented in Sec. 3. The calculated results for the doublet bands, such as energy spectra, electromagnetic transitions, and angular momentum orientations, are discussed in Sec. 4, and a summary is given in Sec. 5.

2. Formalism

The total RAT-PRM Hamiltonian can be expressed as

$$\hat{H} = \hat{H}^{p}_{\text{intr.}} + \hat{H}^{n}_{\text{intr.}} + \hat{H}_{\text{core}}, \tag{1}$$

where $\hat{H}^{p(n)}_{\text{intr.}}$ is the intrinsic Hamiltonian for valence protons (neutrons) in a reflection-asymmetric triaxially deformed potential, and $\hat{H}_{\text{core}}$ is the Hamiltonian of a reflection-asymmetric triaxial rotor, which is generalized straightforwardly from the reflection-asymmetric axial rotor in Ref. [36].

The core Hamiltonian reads

$$\hat{H}_{\text{core}} = \sum_{k=1}^{3} \frac{\hat{R}_k^2}{2\mathcal{J}_k} + \frac{1}{2}E(0^-)(1-\hat{P}), \tag{2}$$

with $\hat{R}_k = \hat{I}_k - \hat{j}_{pk} - \hat{j}_{nk}$. Here, $\hat{R}_k$, $\hat{I}_k$, $\hat{j}_{pk}$, and $\hat{j}_{nk}$ are the angular momentum operators for the core, the nucleus, the valence protons and neutrons, respectively. The moments of inertia for irrotational flow are adopted $\mathcal{J}_k = \mathcal{J}_0 \sin^2(\gamma - 2k\pi/3)$. The core parity splitting parameter $E(0^-)$ can be viewed as the excitation energy of the virtual 0^- state [36]. The core parity operator $\hat{P}$ can be written as the product of the single-particle parity operator $\hat{\pi}$ and the total parity operator $\hat{p}$.

The intrinsic Hamiltonian for valence nucleons is [18,37,38]

$$\begin{aligned}\hat{H}^{p(n)}_{\text{intr.}} &= \hat{H}^{p(n)}_{\text{s.p.}} + \hat{H}_{\text{pair}} \\ &= \sum_{\nu>0}(\varepsilon^{p(n)}_{\nu} - \lambda)(a^{\dagger}_{\nu}a_{\nu} + a^{\dagger}_{\bar{\nu}}a_{\bar{\nu}}) - \frac{\Delta}{2}\sum_{\nu>0}(a^{\dagger}_{\nu}a^{\dagger}_{\bar{\nu}} + a_{\bar{\nu}}a_{\nu}),\end{aligned} \tag{3}$$

where λ denotes the Fermi energy, Δ is the pairing gap parameter, and $|\bar{\nu}\rangle$ is the time-reversal state of $|\nu\rangle$. The single-particle energy $\varepsilon^{p(n)}_{\nu}$ is obtained by diagonalizing the Hamiltonian $\hat{H}^{p(n)}_{\text{s.p.}}$, which has the form of a Nilsson Hamiltonian [39],

$$\hat{H}^{p(n)}_{\text{s.p.}} = -\frac{1}{2}\hbar\omega_0\nabla^2 + V(r;\theta,\varphi) + C\boldsymbol{l}\cdot\boldsymbol{s} + D[\boldsymbol{l}^2 - \langle\boldsymbol{l}^2\rangle_N], \tag{4}$$

with the kinetic energy $-\frac{1}{2}\hbar\omega_0\nabla^2$, the reflection-asymmetric triaxially deformed potential $V(r;\theta,\varphi)$, the spin-orbit term $C\boldsymbol{l}\cdot\boldsymbol{s}$ and the standard $D[\boldsymbol{l}^2 - \langle\boldsymbol{l}^2\rangle_N]$ term [40].

Similar to Ref. [41], the reflection-asymmetric triaxially deformed potential $V(r;\theta,\varphi)$ is written as

$$\begin{aligned}V(r,\theta,\varphi) =& \hbar\omega_0 r^2\Bigg[\frac{1}{2} + \beta_{10}Y_{10} + \beta_{11}\frac{(Y_{11}-Y_{1-1})}{\sqrt{2}} \\ &- \beta_{20}Y_{20} - \beta_{22}\frac{(Y_{22}+Y_{2-2})}{\sqrt{2}} \\ &- \beta_{30}Y_{30} - \beta_{31}\frac{(Y_{31}-Y_{3-1})}{\sqrt{2}} \\ &- \beta_{32}\frac{(Y_{32}+Y_{3-2})}{\sqrt{2}} - \beta_{33}\frac{(Y_{33}-Y_{3-3})}{\sqrt{2}}\Bigg],\end{aligned} \tag{5}$$

with parameters (β_{10},β_{11}), (β_{20},β_{22}), and $(\beta_{30},\beta_{31},\beta_{32},\beta_{33})$ describing the dipole, quadrupole, and octupole deformations, respectively. From the volume conservation and by requiring the center of mass coincided with the origin of the coordinate system, the relations among the parameters can be obtained,

$$\omega_0^2 \approx \left[1 + \frac{5}{16\pi}(\beta_{20}^2 + \beta_{30}^2 + \beta_{22}^2 + \beta_{31}^2 + \beta_{32}^2 + \beta_{33}^2)\right]\mathring{\omega}_0^2, \tag{6}$$

$$\beta_{10} \approx \left[\frac{18\sqrt{3}}{\sqrt{35\pi}}\beta_{20}\beta_{30} + \frac{6\sqrt{3}}{\sqrt{7\pi}}\beta_{22}\beta_{32}\right], \tag{7}$$

$$\beta_{11} \approx \left[\frac{36}{\sqrt{70\pi}}\beta_{20}\beta_{31} + \frac{18}{\sqrt{14\pi}}\beta_{22}\beta_{33} - 12\sqrt{\frac{3}{280\pi}}\beta_{22}\beta_{31}\right]. \tag{8}$$

Here, the higher order terms of (β_{10},β_{11}), (β_{20},β_{22}), and $(\beta_{30},\beta_{31},\beta_{32},\beta_{33})$ are neglected, and $\mathring{\omega}_0$ corresponds to the frequency of an equivalent spherical potential with conserved volume. The parameters β_{20} and β_{22} are related with the commonly used quadrupole deformation parameters β_2 and γ by

$$\beta_{20} = \beta_2\cos\gamma, \quad \beta_{22} = \beta_2\sin\gamma. \tag{9}$$

To include the pairing correlations in RAT-PRM, one should replace the single-particle states $a^{\dagger}_{\nu}|0\rangle$ with the Bardeen-Cooper-Schrieffer (BCS) quasiparticle states $\alpha^{\dagger}_{\nu}|\tilde{0}\rangle$, where $|\tilde{0}\rangle$ is the BCS vacuum,

$$|\tilde{0}\rangle = \prod_{\nu}(u_{\nu} + v_{\nu}a^{\dagger}_{\nu}a^{\dagger}_{\bar{\nu}})|0\rangle, \tag{10}$$

and the quasiparticle operators $\alpha^{\dagger}_{\nu}$ read

$$\begin{pmatrix}\alpha^{\dagger}_{\nu}\\ \alpha_{\bar{\nu}}\end{pmatrix} = \begin{pmatrix}u_{\nu} & -v_{\nu}\\ v_{\nu} & u_{\nu}\end{pmatrix}\begin{pmatrix}a^{\dagger}_{\nu}\\ a_{\bar{\nu}}\end{pmatrix}, \tag{11}$$

with $u_{\nu}^2 + v_{\nu}^2 = 1$. Furthermore, the single-particle energies ε_{ν} should be replaced by quasiparticle energies $\varepsilon'_{\nu} = \sqrt{(\varepsilon_{\nu}-\lambda)^2 + \Delta^2}$. Therefore, the intrinsic Hamiltonian becomes

$$\hat{H}_{\text{intr.}} = \sum_{\nu_p}\varepsilon'_{\nu_p}(\alpha^{\dagger}_{\nu_p}\alpha_{\nu_p} + \alpha^{\dagger}_{\bar{\nu}_p}\alpha_{\bar{\nu}_p}) + \sum_{\nu_n}\varepsilon'_{\nu_n}(\alpha^{\dagger}_{\nu_n}\alpha_{\nu_n} + \alpha^{\dagger}_{\bar{\nu}_n}\alpha_{\bar{\nu}_n}). \tag{12}$$

The Hamiltonian $\hat{H}$ is diagonalized numerically in the symmetrized strong-coupled basis with good parity and angular momentum,

$$|\Psi^{\nu}_{IMK\pm}\rangle = \frac{1}{2\sqrt{1+\delta_{K0}}}(1+\hat{S}_2)|IMK\rangle\psi^{\nu}_{\pm}, \tag{13}$$

where $\hat{S}_2 = \hat{P}\hat{R}_2$ is the reflection operator with respect to the plane perpendicular to 2-axis, $|IMK\rangle = \sqrt{\frac{2\pi+1}{8\pi^2}}D^{I*}_{MK}$ is the Wigner function, $\psi^{\nu}_{\pm}$ are the intrinsic wavefunctions with good parity,

$$\psi^{\nu}_{+} = (1+\hat{p})\tilde{\chi}^{\nu}_{p}\tilde{\chi}^{\nu}_{n}\Phi_a = (1+\hat{P}\hat{\pi}_p\hat{\pi}_n)\tilde{\chi}^{\nu}_{p}\tilde{\chi}^{\nu}_{n}\Phi_a, \tag{14}$$

$$\psi^{\nu}_{-} = (1-\hat{p})\tilde{\chi}^{\nu}_{p}\tilde{\chi}^{\nu}_{n}\Phi_a = (1-\hat{P}\hat{\pi}_p\hat{\pi}_n)\tilde{\chi}^{\nu}_{p}\tilde{\chi}^{\nu}_{n}\Phi_a. \tag{15}$$

Here $\tilde{\chi}^{\nu}_{p}\tilde{\chi}^{\nu}_{n}\Phi_a$ is the strong-coupled intrinsic core-quasiparticle wavefunction; Φ_a represents that the core has the same orientation in space as the intrinsic single-particle potential, and $\tilde{\chi}^{\nu}_{p(n)}$ is the BCS quasiparticle state of the proton (neutron).

The diagonalization of the Hamiltonian $\hat{H}$ gives rise to the nuclear eigenstate,

$$|IMp\rangle = \sum_{\nu K} c^{\nu}_{IKp}|\Psi^{\nu}_{IMKp}\rangle, \quad p = \pm, \tag{16}$$

which is a composition of the strong-coupled basis with the coefficients c^{ν}_{IKp}. Then, the reduced electromagnetic transition probabilities can be calculated via [42]

$$B(\sigma\lambda, I_i \to I'_f) = \frac{1}{2I+1}\sum_{\mu M'} |\langle I'M'p'|\mathcal{M}^{\sigma}_{\lambda\mu}|IMp\rangle|^2, \tag{17}$$

where σ denotes either E or M for electric and magnetic transitions, respectively, λ is the rank of the transition operator, and $\mathcal{M}^{\sigma}_{\lambda\mu}$ the electromagnetic transition operator.

The magnetic dipole ($M1$) transition operator is

$$\hat{\mathcal{M}}(M1,\mu) = \sqrt{\frac{3}{4\pi}}\frac{e\hbar}{2Mc}\Big[(g_p - g_R)\hat{j}^p_{1\mu} + (g_n - g_R)\hat{j}^n_{1\mu}\Big], \tag{18}$$

where g_p, g_n, and g_R are the effective gyromagnetic ratios for valence proton, valence neutron, and the collective core, respectively, and $\hat{j}_{1\mu}$ denotes the spherical tensor in the laboratory frame. The electric multipole transition operators contain two terms [40],

$$\begin{aligned}\hat{\mathcal{M}}(E\lambda,\mu) &= \hat{q}^{(c)}_{\lambda\mu} + \hat{q}^{(p)}_{\lambda\mu} \\ &= \frac{3Ze}{4\pi}R^{\lambda}_0\beta_{\lambda\mu} + e\sum_{i=1}^{n}(\frac{1}{2} - t^{(i)}_3)r^{\lambda}_i Y^*_{\lambda\mu},\end{aligned} \tag{19}$$

which are contributions from the core and the valence particles, respectively. Here, $R_0 = 1.2A^{1/3}$ fm is the nuclear radius. For electric quadrupole ($E2$) transitions, one can safely neglect the valence particle term, since it is much smaller than the term of the core [40]. However, this is not the case for $E1$ transitions. Since the total center of mass remains at rest, the motion of the valence particles is influenced by the recoil of the core. This effect is of special importance for $E1$ transitions. Therefore, as in Ref. [42], the total moment in a one-particle transition is obtained by replacing the charge of the particle by an effective one,

$$e_{\text{eff}} = e\left[\frac{N-Z}{2A} - t^{(i)}_3\right], \tag{20}$$

where $t^{(i)}_3 = +1/2$ or $-1/2$ for neutrons or protons, respectively. An additional contribution to e_{eff} is contained in the polarization term caused by the coupling of the dipole mode to the single-particle motion [36,42]. This contribution combined with the recoil effect one (20), yields the total effective charge for $E1$ transitions

$$e_{\text{eff}} = e\left[\frac{N-Z}{2A} - t^{(i)}_3\right]\times\left[1 - 0.7\frac{(\hbar\omega)^2}{(\hbar\omega)^2 - E^2_{\gamma}}\right], \tag{21}$$

where $\hbar\omega$ is the giant resonance energy, $78A^{-1/3}$ MeV, and E_{γ} is the $E1$ transition energy.

3. Numerical details

The microscopic multidimensionally-constrained covariant density functional theory (MDC-CDFT) [43–45] with PC-PK1 [46] gives the quadrupole deformation $\beta_2 = 0.28$, $\gamma = 16.3°$, and the octupole deformation $\beta_3 = 0$ for the configuration $\pi g_{9/2} \otimes \nu g_{9/2}$ in ^{78}Br. As the potential energy surface is soft with respect to β_3, $\beta_3 = 0.02$ is adopted to include the effect of octupole correlations in the present RAT-PRM calculations.

With the deformation parameters above, the reflection-asymmetric triaxial Nilsson Hamiltonian with the parameters κ, μ in Ref. [47] is solved by expanding the wavefunction by harmonic oscillator basis [48]. The Fermi energies of proton and neutron

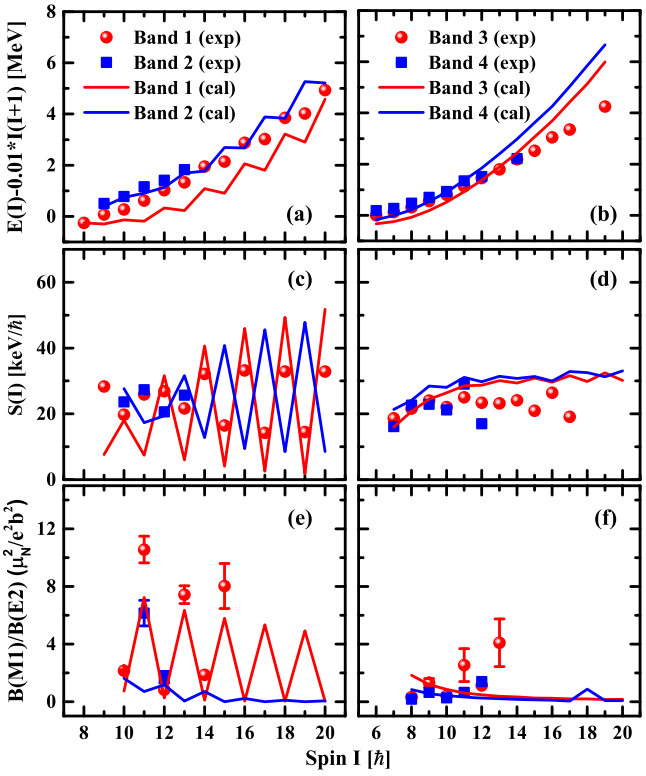

Fig. 1. The excitation energies $E(I)$ [panels (a) and (b)], the energy staggering parameters $S(I) = [E(I) - E(I-1)]/2I$ [panels (c) and (d)], and the $B(M1)/B(E2)$ ratios [panels (e) and (f)] for the positive-parity doublet bands 1 and 2 (left panels) as well as the negative-parity doublet bands 3 and 4 (right panels) in ^{78}Br by RAT-PRM (lines) in comparison with the data available [11] (symbols). The energies are relative to the bandhead of band 1 at $I = 8\hbar$, with a rotor reference subtracted.

are chosen as $\lambda_p = 44.6$ MeV and $\lambda_n = 47.6$ MeV, corresponding to the $\pi g_{9/2}[m_z = 1/2]$ and $\nu g_{9/2}[m_z = 5/2]$ orbitals respectively, which are consistent with the MDC-CDFT results. The single-particle space is truncated to 13 levels, with six above and below the Fermi level. Increasing the size of the single-particle space does not influence the band structure in the present work. The pairing correlation is taken into account by the empirical pairing gap formula $\Delta = 12/\sqrt{A}$ MeV.

The moment of inertia $\mathcal{J}_0 = 14\ \hbar^2$/MeV and the core parity splitting parameter $E(0^-) = 3$ MeV, are adjusted to the experimental energy spectra. For the calculations of magnetic transitions, the gyromagnetic ratios for the collective rotor, protons, and neutrons are given by $g_R = Z/A$, $g_{p(n)} = g_l + (g_s - g_l)/(2l+1)$, respectively [40,42].

4. Results and discussion

In Fig. 1, the excitation energies, the energy staggering parameters $S(I) = [E(I) - E(I-1)]/2I$, and the $B(M1)/B(E2)$ ratios calculated by the RAT-PRM for the positive-parity doublet bands 1 and 2 as well as the negative-parity doublet bands 3 and 4 are shown in comparison with the data available [11]. It is found that the configuration for the positive-parity doublet bands 1 and 2 is $\pi g_{9/2} \otimes \nu g_{9/2}$, while for the negative-parity doublet bands 3 and 4 is $\pi g_{9/2} \otimes \nu f_{5/2}$. It is noted that the positive- and negative-parity doublet bands in ^{78}Br cannot be considered as chirality-parity quartet bands [2], since their configurations are different. A chirality-parity quartet should be based on a single configuration.

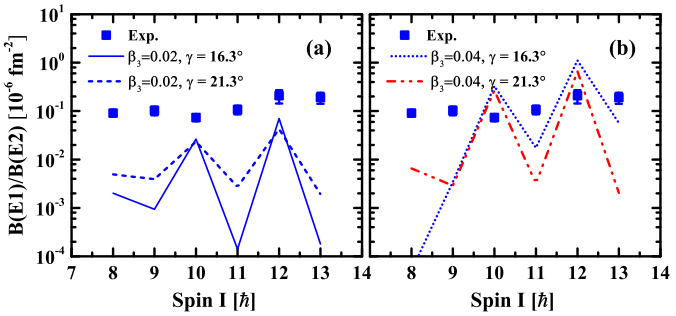

Fig. 2. The calculated $B(E1)/B(E2)$ ratios between the interband $E1$ transitions (band 3 → 1) and the intraband $E2$ transitions (band 3) in comparison with the available data [11] for (a) $\beta_3 = 0.02$ and (b) $\beta_3 = 0.04$.

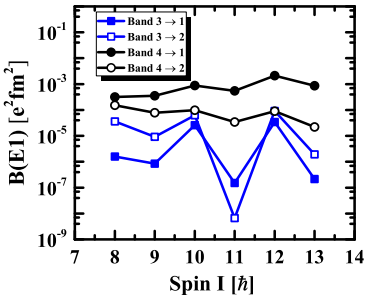

Fig. 3. The calculated interband $E1$ transitions (band 3 → 1), (band 3 → 2), (band 4 → 1), and (band 4 → 2) as functions of spin.

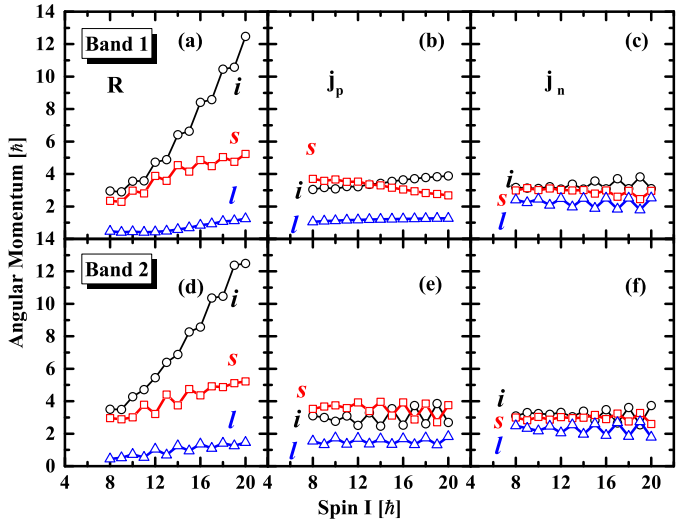

Fig. 4. The angular momenta components along the intermediate (i, circles), short (s, squares), and long (l, triangles) axes for the core $R_k = \langle \hat{R}_k^2 \rangle^{1/2}$ [panels (a) and (d)], valence proton $j_{pk} = \langle \hat{j}_{pk}^2 \rangle^{1/2}$ [panels (b) and (e)], and valence neutron $j_{nk} = \langle \hat{j}_{nk}^2 \rangle^{1/2}$ [panels (c) and (f)] in RAT-PRM for the positive-parity doublet bands 1 and 2.

As shown in Figs. 1(a) and 1(b), the calculated excited energies reproduce the data for the positive-parity doublet bands satisfactorily, and for the negative-parity doublet bands well. Within the spin region $9\hbar \leq I \leq 13\hbar$, the average energy difference for the positive-parity doublet bands is 0.99 MeV, which overestimates the data by ∼0.5 MeV. Within the spin region $6\hbar \leq I \leq 14\hbar$, the average energy difference for the negative-positive doublet bands is 0.35 MeV, which overestimates the data by ∼0.2 MeV. The overestimation of the energy splittings between doublet bands may be due to the small triaxial deformation ($\gamma = 16.3°$) adopted in the present calculations. In Ref. [49], the cranked-shell-model calculations suggest the deformation parameters $(\beta_2, \gamma) = (0.32, 21.3°)$ for band 1 in order to match the experimental moments of inertia. The tilted axis cranking CDFT (TAC-CDFT) calculations [24, 50–54] indicate that the triaxial deformation increases with the rotational frequency. By using a larger triaxial deformation, the RAT-PRM calculations could provide smaller average energy difference for the positive-parity doublet bands and the negative-parity doublet bands.

Figs. 1(c) and 1(d) depict the calculated $S(I)$ values in comparison with the data. For the positive-parity doublet bands, the calculated $S(I)$ values exhibit an odd-even staggering behavior. For the negative-parity doublet bands, the calculated $S(I)$ values are smooth till $14\hbar$. The different $S(I)$ behaviors may be attributed to their corresponding configurations. The proton configurations are similar for both positive- and negative-parity bands, i.e., a particle at the bottom of the $g_{9/2}$ shell. The neutron configurations, however, are quite different. There is a neutron hole at the top of the $f_{5/2}$ shell for the negative-parity bands, but a neutron at the middle of the $g_{9/2}$ shell for the positive-parity bands. For the latter, the neutron alignments along the direction of the collective rotation may occur, and the $S(I)$ staggering appears.

The experimental $B(M1)/B(E2)$ ratios for both positive- and negative-parity doublet bands, including the odd-even staggering for the positive-parity, are well reproduced, as shown in Figs. 1(e) and 1(f). The similarity of $B(M1)/B(E2)$ ratios between the doublet bands is an indication for nuclear chirality as suggested in Ref. [55].

Since the octupole degree of freedom is included in the present RAT-PRM calculations, the electric dipole transition probabilities $B(E1)$ between the positive- and negative-parity bands can be calculated. In Fig. 2(a), the calculated $B(E1)/B(E2)$ ratios between the interband $E1$ transitions (band 3 → 1) and the intraband $E2$ transitions (band 3) are shown in comparison with the available data [11]. In general, the calculated $B(E1)/B(E2)$ ratios underestimate the experimental data. Considering the fact that the calculated $B(M1)/B(E2)$ ratios for band 3 agree with the data, the underestimation of the calculated $B(E1)/B(E2)$ ratios may result from too small $B(E1)$ values.

It is found that both the triaxial deformation γ and octupole deformation β_3 influence the calculated $B(E1)$ values. For $\beta_3 = 0.02$ as shown in Fig. 2(a), the $B(E1)$ values are enhanced by changing γ from 16° to 21° (given by cranked-shell-model calculations [49]). The same calculations with $\beta_3 = 0.04$ have no significant influence on the excited energies, staggering parameters, and $B(M1)/B(E2)$ ratios except the $B(E1)$ values. As shown in Fig. 2(b), the $B(E1)$ values are enhanced with $\beta_3 = 0.04$ and a better agreement with the $B(E1)/B(E2)$ data can be obtained.

In Fig. 3, the calculated interband $E1$ transitions (band 3 → 1), (band 3 → 2), (band 4 → 1), and (band 4 → 2) as functions of spin are given. For both bands 3 and 4, the interband $E1$ transitions to band 1 and band 2 show similar variation patterns as expected for chiral structure. However, the $E1$ transition strengthes from band 4 to bands 1 and 2 are larger than those from band 3.

In order to investigate the chiral geometry, the angular momentum components for the core $R_k = \langle \hat{R}_k^2 \rangle^{1/2}$, the valence proton $j_{pk} = \langle \hat{j}_{pk}^2 \rangle^{1/2}$, and the valence neutron $j_{nk} = \langle \hat{j}_{nk}^2 \rangle^{1/2} (k = 1, 2, 3)$ are presented in Figs. 4 and 5 for the positive- and negative-parity doublet bands, respectively. For the triaxial deformation $\gamma = 16.3°$ adopted here, the intrinsic axes 1, 2, and 3 are respectively the intermediate (i), short (s) and long (l) axes, and the relation of the corresponding moments of inertia is $\mathcal{J}_1 > \mathcal{J}_2 > \mathcal{J}_3$. Therefore, as shown in Figs. 4 and 5, the angular momentum for the core mainly

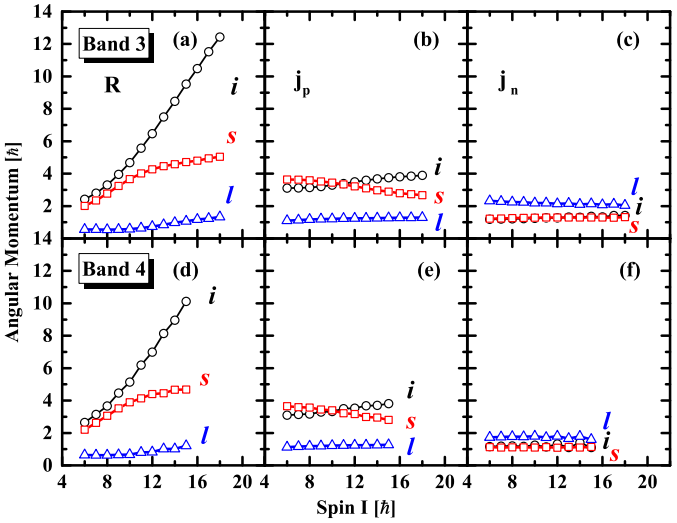

Fig. 5. Same as Fig. 4, but for the negative-parity doublet bands 3 and 4.

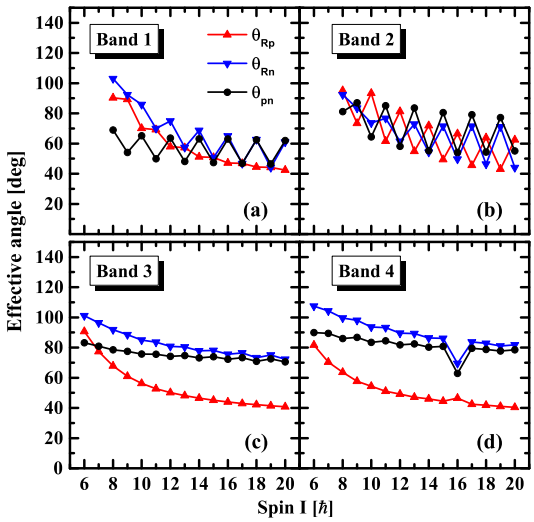

Fig. 6. The effective angles θ_{Rp} (triangle ups), θ_{Rn} (triangle downs) and θ_{pn} (circles) for the positive- [panels (a) and (b)] and negative-parity doublet bands [panels (c) and (d)] as functions of spin.

aligns along the i-axis for both positive- and negative-parity doublet bands.

For the positive-parity doublet bands in Fig. 4, the angular momentum of the valence proton mainly aligns in the i-s plane, while that of the valence neutron has nearly equal components on the three axes due to its mid-shell nature. Considering the fact that the angular momentum for the core mainly aligns along the i-axis, and grows rapidly, the total angular momentum lies close to the i-s plane, which is consistent with the large energy difference between the doublet bands. For band 1, the three components of j_p for the valence proton vary smoothly with the spin, while the three components of j_n for the valence neutron exhibit staggering with $I > 12\hbar$. For band 2, the three components of both j_p and j_n exhibit staggering with $I \geq 9\hbar$. These staggering behaviors might be understood from the main components of the intrinsic wavefunction $\tilde{\chi}_{p(n)}$. It is found that these staggering behaviors are associated with the variation of the corresponding main components. Taking band 1 as an example, with $I > 12\hbar$, the main component of the neutron intrinsic wavefunction varies alternately between $g_{9/2}[m_z = 5/2]$ and $g_{9/2}[m_z = 3/2]$.

For the negative-parity doublet bands in Fig. 5, the angular momentum of the valence proton mainly aligns in the i-s plane, and the alignment of the valence neutron along the l-axis is significant. To be more precise, $j_p \sim 4\hbar$ in the i-s plane, $j_n \sim 2\hbar$ along l-axis, and $R \sim 2\hbar - 13\hbar$ along i-axis. This is the chiral geometry for the negative-parity doublet bands. As the total angular momentum increases, R increases gradually, j_n remains almost unchanged, while j_p moves gradually toward the i-axis. The difference between the proton and neutron alignments may result from the fact that the Coriolis alignment effects are weaker for the neutron in the relatively low-j $f_{5/2}$ shell. It is found that for both band 3 and band 4, the three components of j_p and j_n vary smoothly with the spin. This is different from the case of band 1 and band 2, because the main components here are always $g_{9/2}[m_z = 1/2]$ for proton and $f_{5/2}[m_z = 5/2]$ for neutron.

In Fig. 6, the calculated effective angles θ_{Rp}, θ_{Rn} and θ_{pn} as functions of spin for the positive- and negative-parity doublet bands are presented. The effective angle θ_{pn} between the angular momenta of the proton $\boldsymbol{j}_p$ and neutron $\boldsymbol{j}_n$ is defined as [56]

$$\cos\theta_{pn} = \frac{\langle \boldsymbol{j}_p \cdot \boldsymbol{j}_n \rangle}{\sqrt{\langle j_p^2 \rangle \langle j_n^2 \rangle}}. \tag{22}$$

A similar expression for the effective angle $\theta_{Rp}(\theta_{Rn})$ between the angular momenta for the core and the valence proton (neutron) can be defined straightforwardly.

In Fig. 6, the three effective angles for both the positive- and negative-parity doublet bands decrease with spin. This behavior can be well understood because both the valence proton and the valence neutron gradually align along the direction of the collective rotation with spin. For the positive-parity doublet bands, θ_{Rp} and θ_{Rn} decrease with spin with almost the same slope. This is because the Coriolis alignment effects for the valence proton in $\pi g_{9/2}$ and the valence neutron in $\nu g_{9/2}$ are similar. In contrast, for the negative-parity doublet bands, θ_{Rp} decreases faster than θ_{Rn} with spin. This is because the Coriolis alignment effects for the valence proton in $g_{9/2}$ are stronger than those for the valence neutron in relatively low-j $f_{5/2}$ orbitals.

The effective angles oscillate with spin for the positive-parity doublet bands, while smoothly change with spin for the negative-parity doublet bands except a kink at $I = 16\hbar$ in band 4. The staggering features for bands 1 and 2 are again connected with the change for the main component in the intrinsic wavefunctions, as discussed above. For bands 3 and 4, the main components in the intrinsic wavefunctions, $\pi g_{9/2}[m_z = 1/2]$ and $\nu f_{5/2}[m_z = 5/2]$, are nearly unchanged, which result in the smooth change of the effective angles. In addition, the kink at $I = 16\hbar$ for band 4 is due to a sudden change of the main component in the intrinsic wavefunctions, from $\pi g_{9/2} \otimes \nu f_{5/2}$ to $\pi g_{9/2} \otimes \nu g_{9/2}$.

Finally, a few remarks on the effective angles near the bandheads are appropriate. In Ref. [57], the paradox, i.e., the effective angles between any two of the angular momentum components are closed to 90° in the regime of chiral vibration, has been clarified. This paradox is due to the fact that the angular momentum of the rotor is much smaller than those of the proton and neutron near the bandhead. Here, the three effective angles near the bandheads, in the regime of chiral vibration, are close to 90° for positive-parity band 2, and negative-parity doublet bands 3 and 4. However, the effective angle θ_{pn} at the bandhead for band 1 is only 70° due to the deviation from the ideal particle-hole configuration and triaxial deformation.

It should be noted that for the negative-parity doublet bands the previous adopted configuration is $\pi f_{5/2} \otimes \nu g_{9/2}$ [11]. In the present calculations, the configuration $\pi g_{9/2} \otimes \nu g_{9/2}$ same as in Ref. [11] is adopted for the positive-parity doublet bands. After in-

cluding the octupole deformation, the positive- and negative-parity bands can be simultaneously obtained by diagonalizing the RAT-PRM Hamiltonian. For the yrast band with negative parity, the configuration is found to be $\pi g_{9/2} \otimes \nu f_{5/2}$. Further support for this subtle change in configuration for the negative-parity doublet bands may be obtained from future microscopic calculations and experimental results, for example, the three-dimensional TAC-CDFT [24] including the octupole deformation or the measurement of the g factor in the chiral bands [58].

5. Summary

In summary, a reflection-asymmetric triaxial particle rotor model (RAT-PRM) with a quasi-proton and a quasi-neutron coupled with a reflection-asymmetric triaxial rotor is developed and applied to the MχD candidates with octupole correlations in ^{78}Br.

The excited energies, energy staggering parameters $S(I) = [E(I) - E(I-1)]/2I$ and $B(M1)/B(E2)$ ratios are calculated for the positive-parity doublet bands 1 and 2 as well as the negative-parity doublet bands 3 and 4. Since the octupole deformation is included in the present RAT-PRM calculations, the electric dipole transition probabilities $B(E1)$ between the positive- and negative-parity bands can be calculated. The calculated excited energies and the energy staggering parameters reproduce the data for the positive-parity doublet bands satisfactorily, and for the negative-parity doublet bands well. The calculated $B(M1)/B(E2)$ ratios agree well with the experimental data, while the calculated $B(E1)/B(E2)$ ratios underestimate the data in general. It is found that both the triaxial deformation γ and octupole deformation β_3 influence the calculated $B(E1)$ values. For $\beta_3 = 0.02$, the $B(E1)$ values are enhanced by changing γ from 16° to 21° (given by cranked-shell-model calculations [49]). The same calculations with $\beta_3 = 0.04$ have no significant influence on the excited energies, staggering parameters, and $B(M1)/B(E2)$ ratios except the $B(E1)$ values. The $B(E1)$ values are enhanced with $\beta_3 = 0.04$ and a better agreement with the $B(E1)/B(E2)$ data can be obtained.

The chiral geometry and its evolution are discussed in details from the angular momentum components for the core as well as the valence proton and neutron. For the positive-parity doublet bands, in consistent with the large energy difference between the doublet bands, the total angular momentum lying close to the i-s plane. For the negative-parity doublet bands, the chiral geometry is constructed by the angular momenta of the valence proton along the i-s plane, the valence neutron along the l-axis, and the core along the i-axis.

Acknowledgements

This work was partly supported by the National Key R&D Program of China (Contract No. 2018YFA0404400 and No. 2017YFE0116700), the National Natural Science Foundation of China (Grants No. 11621131001 and No. 11875075).

References

[1] S. Frauendorf, J. Meng, Nucl. Phys. A 617 (1997) 131.
[2] S. Frauendorf, Rev. Mod. Phys. 73 (2001) 463.
[3] J. Meng, S.Q. Zhang, J. Phys. G 37 (2010) 064025.
[4] J. Meng, P.W. Zhao, Phys. Scr. 91 (2016) 053008.
[5] A.A. Raduta, Prog. Part. Nucl. Phys. 90 (2016) 241.
[6] K. Starosta, T. Koike, Phys. Scr. 92 (2017) 093002.
[7] S. Frauendorf, Phys. Scr. 93 (2018) 043003.
[8] J. Meng, J. Peng, S.Q. Zhang, S.G. Zhou, Phys. Rev. C 73 (2006) 37303.
[9] A.D. Ayangeakaa, U. Garg, M.D. Anthony, S. Frauendorf, J.T. Matta, B.K. Nayak, D. Patel, Q.B. Chen, S.Q. Zhang, P.W. Zhao, B. Qi, J. Meng, R.V.F. Janssens, M.P. Carpenter, C.J. Chiara, F.G. Kondev, T. Lauritsen, D. Seweryniak, S. Zhu, S.S. Ghugre, R. Palit, Phys. Rev. Lett. 110 (2013) 172504.
[10] I. Kuti, Q.B. Chen, J. Timár, D. Sohler, S.Q. Zhang, Z.H. Zhang, P.W. Zhao, J. Meng, K. Starosta, T. Koike, E.S. Paul, D.B. Fossan, C. Vaman, Phys. Rev. Lett. 113 (2014) 032501.
[11] C. Liu, S.Y. Wang, R.A. Bark, S.Q. Zhang, J. Meng, B. Qi, P. Jones, S.M. Wyngaardt, J. Zhao, C. Xu, S.-G. Zhou, S. Wang, D.P. Sun, L. Liu, Z.Q. Li, N.B. Zhang, H. Jia, X.Q. Li, H. Hua, Q.B. Chen, Z.G. Xiao, H.J. Li, L.H. Zhu, T.D. Bucher, T. Dinoko, J. Easton, K. Juhász, A. Kamblawe, E. Khaleel, N. Khumalo, E.A. Lawrie, J.J. Lawrie, S.N.T. Majola, S.M. Mullins, S. Murray, J. Ndayishimye, D. Negi, S.P. Noncolela, S.S. Ntshangase, B.M. Nyakó, J.N. Orce, P. Papka, J.F. Sharpey-Schafer, O. Shirinda, P. Sithole, M.A. Stankiewicz, M. Wiedeking, Phys. Rev. Lett. 116 (2016) 112501.
[12] C.M. Petrache, B.F. Lv, A. Astier, E. Dupont, Y.K. Wang, S.Q. Zhang, P.W. Zhao, Z.X. Ren, J. Meng, P.T. Greenlees, H. Badran, D.M. Cox, T. Grahn, R. Julin, S. Juutinen, J. Konki, J. Pakarinen, P. Papadakis, J. Partanen, P. Rahkila, M. Sandzelius, J. Saren, C. Scholey, J. Sorri, S. Stolze, J. Uusitalo, B. Cederwall, O. Aktas, A. Ertoprak, H. Liu, S. Matta, P. Subramaniam, S. Guo, M.L. Liu, X.H. Zhou, K.L. Wang, I. Kuti, J. Timár, A. Tucholski, J. Srebrny, C. Andreoiu, Phys. Rev. C 97 (2018) 041304.
[13] T. Roy, G. Mukherjeea, M. Asgara, S. Bhattacharyyaa, S. Bhattacharyaa, C. Bhattacharyaa, S. Bhattacharyaa, T. Ghosha, K. Banerjeea, S. Kundua, T. Rana, P. Roya, R. Pandeya, J. Meena, A. Dhal, R. Palitd, S. Saha, J. Sethi, S. Thakur, B. Naidu, S. Jadav, R. Dhonti, H. Pai, A. Goswami, Phys. Lett. B 782 (2018) 768.
[14] B.W. Xiong, Y.Y. Wang, At. Data Nucl. Data Tables 125 (2019) 193.
[15] M. Wang, Y.Y. Wang, L.H. Zhu, B.H. Sun, G.L. Zhang, L.C. He, W.W. Qu, F. Wang, T.F. Wang, Y.Y. Chen, C. Xiong, J. Zhang, J.M. Zhang, Y. Zheng, C.Y. He, G.S. Li, J.L. Wang, X.G. Wu, S.H. Yao, C.B. Li, H.W. Li, S.P. Hu, J.J. Liu, Phys. Rev. C 98 (2018) 014304.
[16] J. Peng, J. Meng, S.Q. Zhang, Phys. Rev. C 68 (2003) 044324.
[17] T. Koike, K. Starosta, I. Hamamoto, Phys. Rev. Lett. 93 (2004) 172502.
[18] S.Q. Zhang, B. Qi, S.Y. Wang, J. Meng, Phys. Rev. C 75 (2007) 044307.
[19] B. Qi, S.Q. Zhang, J. Meng, S.Y. Wang, S. Frauendorf, Phys. Lett. B 675 (2009) 175.
[20] Q.B. Chen, B.F. Lv, C.M. Petrache, J. Meng, Phys. Lett. B 782 (2018) 744.
[21] V.I. Dimitrov, S. Frauendorf, F. Dönau, Phys. Rev. Lett. 84 (2000) 5732.
[22] P. Olbratowski, J. Dobaczewski, J. Dudek, W. Plóciennik, Phys. Rev. Lett. 93 (2004) 052501.
[23] P. Olbratowski, J. Dobaczewski, J. Dudek, Phys. Rev. C 73 (2006) 84.
[24] P.W. Zhao, Phys. Lett. B 773 (2017) 1.
[25] S. Mukhopadhyay, D. Almehed, U. Garg, S. Frauendorf, T. Li, P.V.M. Rao, X. Wang, S.S. Ghugre, M.P. Carpenter, S. Gros, Phys. Rev. Lett. 99 (2007) 172501.
[26] D. Almehed, F. Dönau, S. Frauendorf, Phys. Rev. C 83 (2011) 1168.
[27] Q.B. Chen, S.Q. Zhang, P.W. Zhao, R.V. Jolos, J. Meng, Phys. Rev. C 87 (2013) 024314.
[28] Q.B. Chen, S.Q. Zhang, P.W. Zhao, R.V. Jolos, J. Meng, Phys. Rev. C 94 (2016).
[29] X.H. Wu, Q.B. Chen, P.W. Zhao, S.Q. Zhang, J. Meng, Phys. Rev. C 98 (2018) 064302.
[30] S. Brant, D. Tonev, G. De Angelis, A. Ventura, Phys. Rev. C 78 (2008) 034301.
[31] A.A. Raduta, A.H. Raduta, C.M. Petrache, J. Phys. G 43 (2016) 095107.
[32] K. Hara, Y. Sun, Int. J. Mod. Phys. E 04 (1995) 637.
[33] G.H. Bhat, R.N. Ali, J.A. Sheikh, R. Palit, Nucl. Phys. A 922 (2014) 150.
[34] F.Q. Chen, Q.B. Chen, Y.A. Luo, J. Meng, S.Q. Zhang, Phys. Rev. C 96 (2017) 051303.
[35] F.Q. Chen, J. Meng, S.Q. Zhang, Phys. Lett. B 785 (2018) 211.
[36] G.A. Leander, R.K. Sheline, Nucl. Phys. A 413 (1984) 375.
[37] I. Hamamoto, Nucl. Phys. A 271 (1976) 15.
[38] I. Hamamoto, B. Mottelson, Phys. Lett. B 127 (1983) 281.
[39] S.G. Nilsson, Mat.-Fys. Medd. Dan. Vid. Selsk 29 (1955) 1.
[40] P. Ring, P. Schuck, The Nuclear Many-Body Problem, Springer Science & Business Media, 2004.
[41] I. Hamamoto, B. Mottelson, H. Xie, X.Z. Zhang, Z. Phys. D 21 (1991) 163.
[42] A. Bohr, B.R. Mottelson, Nuclear Structure, vol. ii, 1975.
[43] B.N. Lu, E.G. Zhao, S. Zhou, Phys. Rev. C 85 (2012) 011301.
[44] J. Zhao, B.N. Lu, E.G. Zhao, S.G. Zhou, Phys. Rev. C 86 (2012) 057304.
[45] B.N. Lu, J. Zhao, E.G. Zhao, S.G. Zhou, Phys. Rev. C 89 (2014) 014323.
[46] P.W. Zhao, Z.P. Li, J.M. Yao, J. Meng, Phys. Rev. C 82 (2010) 054319.
[47] S.G. Nilsson, C.F. Tsang, A. Sobiczewski, Z. Szymański, S. Wycech, C. Gustafson, I.-L. Lamm, P. Möller, B. Nilsson, Nucl. Phys. A 131 (1969) 1.
[48] Y.Y. Wang, Z.X. Ren, Sci. China, Phys. Mech. Astron. 61 (2018) 082012.
[49] E. Landulfo, D.F. Winchell, J.X. Saladin, F. Cristancho, D.E. Archer, J. Doring, G.D. Johns, M.A. Riley, S.L. Tabor, V.A. Wood, S. Salem-Vasconcelos, O. Dietzsch, Phys. Rev. C 54 (1996) 626.
[50] P.W. Zhao, S.Q. Zhang, J. Peng, H.Z. Liang, P. Ring, J. Meng, Phys. Lett. B 699 (2011) 181.
[51] P.W. Zhao, J. Peng, H.Z. Liang, P. Ring, J. Meng, Phys. Rev. Lett. 107 (2011) 122501.
[52] J. Meng, J. Peng, S.Q. Zhang, P.W. Zhao, Front. Phys. 8 (2013) 55.
[53] P.W. Zhao, N. Itagaki, J. Meng, Phys. Rev. Lett. 115 (2015) 022501.
[54] P.W. Zhao, Z.P. Li, Int. J. Mod. Phys. E 27 (2018) 1830007.
[55] S.Y. Wang, S.Q. Zhang, B. Qi, J. Meng, Chin. Phys. Lett. 24 (2007) 664.

[56] K. Starosta, C.J. Chiara, D.B. Fossan, T. Koike, T.T.S. Kuo, D.R. LaFosse, S.G. Rohozinski, C. Droste, T. Morek, J. Srebrny, Phys. Rev. C 65 (2002) 044328.
[57] Q.B. Chen, J. Meng, Phys. Rev. C 98 (2018) 031303.
[58] E. Grodner, J. Srebrny, C. Droste, L. Próchniak, S.G. Rohoziński, M. Kowalczyk, M. Ionescu-Bujor, C.A. Ur, K. Starosta, T. Ahn, M. Kisieliński, T. Marchlewski, S. Aydin, F. Recchia, G. Georgiev, R. Lozeva, E. Fiori, M. Zielińska, Q.B. Chen, S.Q. Zhang, L.F. Yu, P.W. Zhao, J. Meng, Phys. Rev. Lett. 120 (2018) 022502.